PAPER

Heterogeneous photocatalytic degradation of selected pharmaceutical and personal care products (PPCPs) under visible light using SiO$_2$–TiO$_2$/SnO$_2$: effect of tin precursors and SiO$_2$

Kunyang Li, Yidan Peng, Shuangyu Li, Fengying Luo, Jing Li, Haidong Ju, Yepeng Yang [ID] and Yizhou Li [ID] *

In this study, SiO$_2$–TiO$_2$/SnO$_2$ composites were synthesized using a facile sol–gel method to facilitate the heterogeneous photocatalytic degradation of selected pharmaceuticals and personal care products (PPCPs), namely tetracycline hydrochloride (TC) and ciprofloxacin (CIP), under visible light. The effects of different tin precursors (SnCl$_4$·5H$_2$O, SnCl$_2$ and Na$_2$SnO$_3$·3H$_2$O) along with the addition of SiO$_2$ on photocatalytic performance were systematically evaluated. The photocatalyst prepared by SnCl$_4$·5H$_2$O as the tin precursor showed the highest photodegradation performance for ciprofloxacin (CIP) and tetracycline (TC), and the photodegradation performance for tetracycline (TC) was 1.8, 4.33 and 43.33 times that of SnCl$_2$ and Na$_2$SnO$_3$·3H$_2$O as the tin precursor and pristine TiO$_2$, respectively. Furthermore, the incorporation of SiO$_2$ significantly improved the photocatalytic performance under visible light. The SiO$_2$–TiO$_2$/SnO$_2$ (SnCl$_4$) composites exhibited a 2.65-fold increase in tetracycline (TC) degradation compared to the SiO$_2$-free TiO$_2$–SnO$_2$ (SnCl$_4$) materials. The significant improvement of photocatalytic activity is attributed to the effects of tin precursors and SiO$_2$ on the physicochemical properties, charge carrier dynamics and surface reactivity of the composites. This study presents a novel method for developing composite photocatalysts with exceptional activity by employing various tin precursors and incorporating SiO$_2$ to enhance the removal of pharmaceutical and personal care products (PPCPs) under visible light. The findings have substantial implications for future research in the photocatalytic degradation of PPCPs, fostering environmentally friendly approaches in this field.

1 Introduction

The increasing presence of pharmaceutical and personal care products (PPCPs) in aquatic environments has raised significant concerns due to their potential ecological and human health risks.[1,2] These pollutants, which are usually persistent and biologically active, are often detected in wastewater and surface water. However, traditional treatment processes such as biological treatment, adsorption, filtration and coagulation have limited efficiency in removing these pollutants.[3–6] Advanced oxidation technologies (AOPs), especially photocatalysis, have emerged as a promising strategy for the degradation of PPCPs due to their ability to generate highly reactive oxygen species (ROS) under light irradiation.[7] Among various photocatalysts, titanium dioxide (TiO$_2$) has been widely studied due to its chemical stability, low cost, and strong oxidising ability. However, the rapid charge recombination and wide

band gap (3.2 eV) limit the practical application of titanium dioxide in photocatalysis, particularly under visible light.[8,9]

To enhance the visible light responsiveness and photocatalytic efficiency of TiO$_2$, modifications such as doping, heterostructure construction and composite formation have been explored. Tin oxide (SnO$_2$), characterized by suitable band alignment and high electron mobility, has been used as a coupling agent to improve charge separation in TiO$_2$-based photocatalysts. Petronela Pascariu *et al.* investigated the effects of Sn loading and calcination temperature on the synthesis, structure, optical and catalytic properties of TiO$_2$/SnO$_2$. They found that the highest photocatalytic activity was obtained for the sample with a calcination temperature of 500 °C and a Sn loading of 1.5%.[10] The highest photocatalytic efficiency of TiO$_2$/SnO$_2$ nanotube composite photocatalyst with 5 wt% SnO$_2$ content was shown by Lin-Rui Hou *et al.*[11] The effect of calcination temperature and tin dioxide content on TiO$_2$/SnO$_2$ have been extensively studied by the previous researchers.[10–12] However, investigations into various tin precursors remain limited.

In general, tin(IV) chloride pentahydrate (SnCl$_4$·5H$_2$O), tin(II) chloride (SnCl$_2$), sodium stannate trihydrate (Na$_2$SnO$_3$·3H$_2$O)

Yunnan Key Laboratory of Metal–Organic Molecular Materials and Device, School of Chemistry and Chemical Engineering, Kunming University, Kunming 650214, China. E-mail: zh111111ou@kmu.edu.cn

and tin chloride ($SnCl_4$) have been widely used as tin precursors for the preparation of TiO_2/SnO_2. Kateryna Bila *et al.* investigated the effect of $SnCl_2$ and $SnCl_4$ on TiO_2/SnO_2 composites and showed that the use of divalent tin led to the obtaining of nanocomposites, while the use of tetravalent tin led to the obtaining of solid solutions.[12] Different tin precursors have significant effects on the properties and characteristics of the synthesized TiO_2/SnO_2. These precursors influence the material's specific surface area, the chemical state of tin, and the surface properties, which in turn impact the photocatalytic activity.

Silicon dioxide (SiO_2) also plays an important factor in the preparation of composites. Previous studies have also shown that the specific surface area, surface morphology and optical properties of the materials are significantly influenced by SiO_2.[13] The quantitative deposition of titanium dioxide on silica was found to significantly increase the specific surface area of the materials and enhance the photocatalytic activity by M. Bellardita *et al.*[14] M. r. S. Nivetha *et al.* prepared SiO_2–TiO_2/g-C_3N_4 materials, focusing on the role of SiO_2. They found that SiO_2 enhances the light reflectivity of the sample and reduces the complexation of photogenerated electrons and holes in addition to increasing the specific surface area and refining the grains.[15]

In this study, a simple sol–gel method was developed to synthesize SiO_2–TiO_2/SnO_2 composites by varying the tin precursors and incorporated of SiO_2. The effects of various tin precursors ($SnCl_4 \cdot 5H_2O$, $SnCl_2$ and $Na_2SnO_3 \cdot 3H_2O$) on the physicochemical properties and photocatalytic activities of the composites were systematically evaluated. Furthermore, the influence of SiO_2 addition on the charge carrier dynamics, and surface reactivity was elucidated. The visible light photocatalytic activities of the samples were investigated through the degradation of selected pharmaceuticals and personal care products (PPCPs), specifically tetracycline hydrochloride (TC) and ciprofloxacin (CIP). These findings can be attributed to the differing capabilities of materials synthesized from various tin sources in transferring and delivering electrons during the photocatalytic process, as well as the physicochemical properties and surface reactivity enhanced by the incorporation of SiO_2

2 Experimental section

2.1 Chemicals and reagents

Titanium tetraisopropoxide (TTIP, ≥98%) provided from Adamas-beta. Tin(II) chloride ($SnCl_2$, 99%), tetracycline hydrochloride (TC, 99%), tin(IV) chloride pentahydrate ($SnCl_4 \cdot 5H_2O$, 99%), sodium stannate trihydrate ($Na_2SnO_3 \cdot 3H_2O$, 98%), nitric acid (HNO_3, 65–68%), tetraethyl orthosilicate (TEOS, 98%), ethanol (Et, ≥99.7%), *p*-benzoquinone (BQ, 99%), ciprofloxacin (CIP, 98%) were purchased from Merck. Methanol (MA, ≥99.5%), ammonia solution (NH_4OH, 25%) were purchased from Tianjin Damao Chemical Reagent Partnership Enterprise (Limited Partnership). Ethylenediamine tetraacetic acid disodium salt (EDTA-2Na, ≥99%), isopropanol (IPA, 99.7%) were obtained from Tianjin ZhiYuan Reagent Co.,Ltd. All chemicals

were used without further purification. In addition, deionised water was used for all experiments.

2.2 Catalyst preparation

In a typical procedure, 0.403 g of tin(IV) chloride pentahydrate ($SnCl_4 \cdot 5H_2O$) was dissolved in 35 mL of ethanol (C_2H_5OH). Then, 7.55 mL of tetraethyl silicate (TEOS) and 0.3 mL of concentrated nitric acid (HNO_3) were added to the solution under continuous stirring for 20 minutes. Subsequently, 10 mL of titanium tetraisopropoxide (TTIP) was added dropwise slowly. After stirring for another 20 minutes, a mixture of 15 mL ethanol and 2.5 mL H_2O was added, followed by the addition of 3.5 mL of a methanol/ammonia mixed solution (4 : 1, v/v) to form a homogeneous gel. The gel was aged at room temperature for 48 hours. The as-obtained precursor material was then transferred into a high-temperature and high-pressure reactor and calcined at 265 °C for 2 hours under nitrogen atmosphere. After washing and drying, the intermediate product was further calcined at 40 °C for 4 hours, followed by another washing and drying step to obtain the final SiO_2–TiO_2/SnO_2 ($SnCl_4$) composite material. Using the same synthetic protocol, control materials were prepared by employing tin(II) chloride ($SnCl_2$) and sodium stannate trihydrate (Na_2SnO_3) as tin precursors. All synthesized materials maintained a constant molar ratio of Si : Ti : Sn at 3 : 3 : 0.1.

For comparison, TiO_2 (without SiO_2 and tin precursors), SiO_2–TiO_2 (without tin precursors), SiO_2–SnO_2 ($SnCl_4$) (without TiO_2) and TiO_2/SnO_2 ($SnCl_4$) (without SiO_2) were prepared by similar methods.

3 Results and discussion

3.1 Characterization

The crystalline phases of the synthesized samples were analyzed using X-ray diffraction (XRD). As displayed in Fig. 1, the diffraction peaks at 25.3°, 37.9°, 48.1°, and 55.1° correspond to the anatase crystal phases (101), (004), (200), and (211),
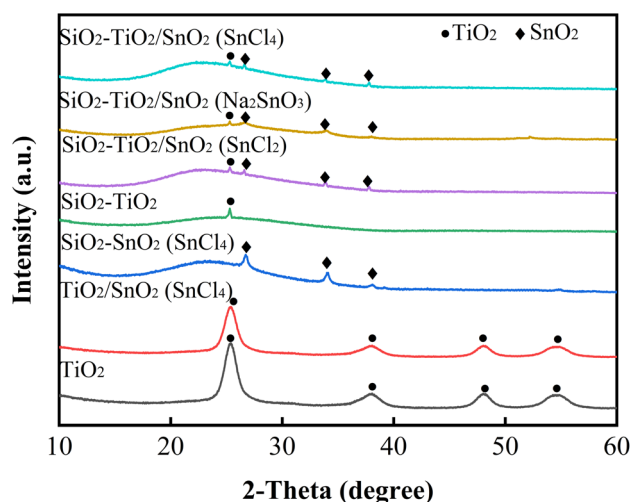

Fig. 1 XRD spectra of prepared samples.

respectively.[16] The broad and weak absorption peaks observed in the 15° to 25° range of the SiO_2-added material can be attributed to the amorphous structure of SiO_2.[17] The diffraction angles of SnO_2 corresponding to (101), (200) and (211) of SnO_2 are 26.6°, 33.9° and 37.8°, respectively.[18] As shown in Fig. 1, diffraction peaks corresponding to SnO_2 were not detected in TiO_2/SnO_2 ($SnCl_4$) samples. However, the addition of SiO_2 resulted in the emergence of distinct diffraction peaks associated with SnO_2. In TiO_2/SnO_2 ($SnCl_4$), the diffraction peaks associated with the anatase phase of TiO_2 are distinctly sharp, indicating a high degree of crystallinity. The absence of detectable diffraction peaks for SnO_2 may be attributed to its relatively low concentration within the TiO_2 matrix, which may be below the detection limit of X-ray diffraction (XRD).[11,19] Following the addition of SiO_2, the relative content of TiO_2 decreases due to the small particle size of samples, which contributes to a reduction in its crystallinity.[20] Consequently, the concentration of SnO_2 increases relatively, making the diffraction peaks of SnO_2 detectable by XRD. A comparison analysis of all samples reveals that the characteristic peak of TiO_2, observed at approximately 25.3°, diminishes following the addition of SiO_2. This reduction can be attributed to both the decrease in TiO_2 content and its crystallinity. Simultaneously, the peaks of SiO_2, TiO_2 and SnO_2 are observed in SiO_2–TiO_2/SnO_2 composites, thereby confirming the successful preparation of these composites.

The FTIR spectra of the materials between 4000 cm^{-1} and 500 cm^{-1} are shown in Fig. 2. The two absorption bands at 3450 cm^{-1} and 1630 cm^{-1} represent the stretching vibrations of the water and hydroxyl groups, respectively.[21] The SiO_2-added material shows three absorption bands at 1080 cm^{-1} and, 955 cm^{-1} and 792 cm^{-1}. They represent the asymmetric telescopic vibration of Si–O–Si, the bending vibration of Si–OH and the symmetric telescopic vibration peak of Si–O, respectively.[20] The absorption band of SiO_2–SnO_2 ($SnCl_4$) at 1080 cm^{-1} is stronger than that of other materials at the same wavenumber.
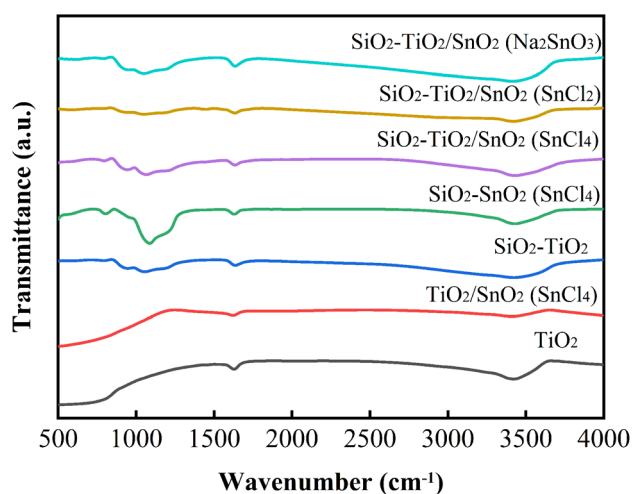
This enhancement can be attributed to the stretching vibration of the Sn–O bond, which may also contribute to the spectral feature near 1080 cm^{-1}. Additionally, the vibrational modes of the Sn–O bond may overlap with those of the Si–O–Si bond, resulting in increased intensity of the absorption band for SiO_2–SnO_2 ($SnCl_4$).[22] The absorption bands at 1080 cm^{-1} for the composites SiO_2–TiO_2/SnO_2 ($SnCl_4$), SiO_2–TiO_2/SnO_2 ($SnCl_2$), and SiO_2–TiO_2/SnO_2 (Na_2SnO_3) are weaker than those of SiO_2–SnO_2 ($SnCl_4$). This attenuation is attributed to the interactions among the three oxides, which induce significant alterations in the electron cloud distribution.[23] As a result, these alterations impact the vibrational properties of the Si–O–Si bond, leading to a reduced dipole moment and a correspondingly weaker absorption band.[23] FT-IR spectra indicate the presence of Sn–O bonds, Si–O bonds, Si–O–Si bond energies in SiO_2–TiO_2/SnO_2 (Na_2SnO_3), SiO_2–TiO_2/SnO_2 ($SnCl_2$) and SiO_2–TiO_2/SnO_2 ($SnCl_4$). Notably, the observed spectral changes show pronounced interactions among the three oxide components. These suggest that SiO_2–TiO_2/SnO_2 composites have been successfully synthesised, while there may be synergistic and other effects among the three components.

The SEM and EDS spectra of these materials are shown in Fig. 3. A comparison of Fig. 3a and b reveals that the TiO_2/SnO_2 ($SnCl_4$) sample exhibits a smooth and compact surface with minimal porosity. In contrast, the SiO_2–TiO_2/SnO_2 ($SnCl_4$) sample, which incorporates additional SiO_2, exhibits a rough and loose texture. The rough surface not only enhances the specific surface area of the catalyst, but also improves light utilization through multiple diffuse reflections.[24] The incorporation of SiO_2 into the samples leads to a looser surface texture, which can significantly enhance their specific surface area. This increase in surface area provides more active sites for both adsorption and photocatalytic processes.[25] The comparison of Fig. 3b–d demonstrates that different tin precursors significantly influence the morphology of the composites. Among the three Sn-based materials analyzed, SiO_2–TiO_2/SnO_2 ($SnCl_4$), synthesized using $SnCl_4 \cdot 5H_2O$ as a precursor, exhibits the most sparse and porous structure, while SiO_2–TiO_2/SnO_2 (Na_2SnO_3), derived from $Na_2SnO_3 \cdot 3H_2O$ as a precursor, is characterized by the highest density. This suggests that different tin precursors may have an effect on the specific surface area of the composites, which affects the photocatalytic effect of the materials. The microscopic chemical ingredient analysis of the SiO_2–TiO_2/SnO_2 ($SnCl_4$) materials has been shown in Fig. 3e. The patterns show the presence of tin (Sn), oxygen (O), silicon (Si) and titanium (Ti) without any other element. Four elements, namely Sn, O, Si and Ti, were identified and their molar percentages were confirmed to be 0.84%, 50.32%, 25.41% and 23.43% respectively. The measured molar percentages of these four elements were consistent with expectations, indicating that SiO_2–TiO_2/SnO_2 ($SnCl_4$) was prepared accurately. Fig. 3f–i shows the elemental profiles of tin (Sn), oxygen (O), silicon (Si) and titanium (Ti) on SiO_2–TiO_2/SnO_2 ($SnCl_4$) with different colours. This homogeneity suggests a well-integrated structure on materials which is crucial for the photocatalysis.[25]

The morphology and microstructure of TiO_2/SnO_2 ($SnCl_4$) and SiO_2–TiO_2/SnO_2 ($SnCl_4$) composites were analysed using

Fig. 2 FT-IR spectra of TiO_2, TiO_2/SnO_2 ($SnCl_4$), SiO_2–TiO_2, SiO_2–SnO_2 ($SnCl_4$), SiO_2–TiO_2/SnO_2 ($SnCl_4$), SiO_2–TiO_2/SnO_2 ($SnCl_2$) and SiO_2–TiO_2/SnO_2 (Na_2SnO_3).
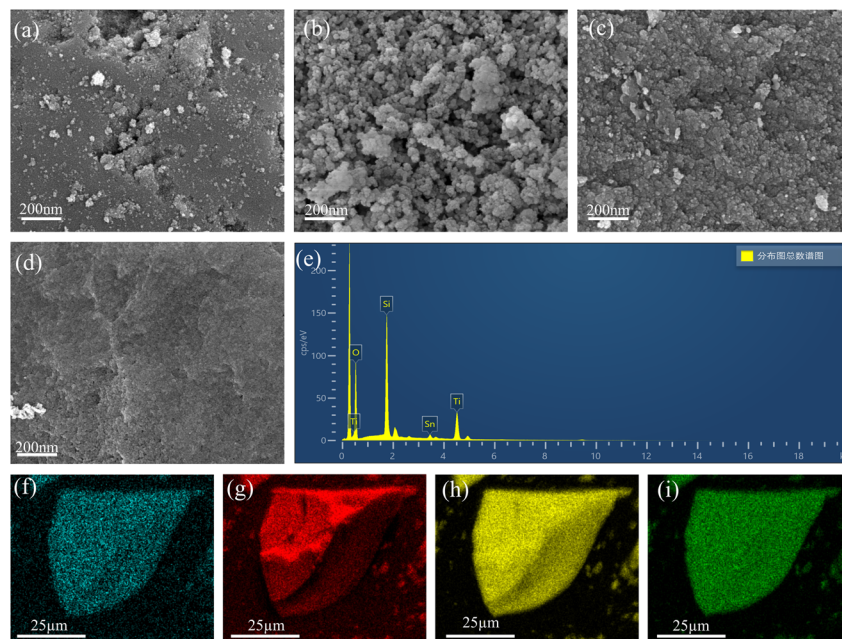
Fig. 3 SEM images of TiO$_2$/SnO$_2$ (SnCl$_4$) (a), SEM images of SiO$_2$–TiO$_2$/SnO$_2$ (SnCl$_4$) (b), SEM images of SiO$_2$–TiO$_2$/SnO$_2$ (SnCl$_2$) (c), SEM images of SiO$_2$–TiO$_2$/SnO$_2$ (Na$_2$SnO$_3$) (d), EDS spectrum of SiO$_2$–TiO$_2$/SnO$_2$ (SnCl$_4$) (e), EDS mapping images of Sn (f), O (g), Si (h), Ti (i).

TEM and HRTEM techniques. In the TEM analysis (Fig. 4a and b), a significant difference in the morphology of TiO$_2$/SnO$_2$ (SnCl$_4$) and SiO$_2$–TiO$_2$/SnO$_2$ (SnCl$_4$) composites can be observed. The TiO$_2$/SnO$_2$ (SnCl$_4$) composite is characterized by the presence of spherical nanoparticles that aggregate to form larger clusters. In contrast, the SiO$_2$–TiO$_2$/SnO$_2$ (SnCl$_4$) composite is characterized by more dispersed spherical nanoparticles, each enveloped by a thin film on the exterior, and this encapsulated film is reported by Yanyan He *et al.* to be possibly SiO$_2$.[26] The HRTEM image in Fig. 4c shows that the stripe spacing is approximately 0.352 nm, indicating that the sample growth direction of the anatase TiO$_2$ (1 0 1) plane.[25]

The N$_2$ adsorption and desorption isotherm curves, as illustrated in Fig. S1 and S2, were recorded to investigate the specific surface area and corresponding pore size distribution of the samples.[27] According to the IUPAC classification of nitrogen adsorption and desorption isotherms, all samples exhibited type IV isotherms, except for SiO$_2$–SnO$_2$ (SnCl$_4$), which displayed type II isotherms. This indicates that the prepared materials possess macroporous and mesoporous

properties. The pore size distribution of all the samples is primarily ranges from 0 to 80 nm, indicating the macroporous and mesoporous properties of the prepared materials. As shown in Table 1, the incorporation of SiO$_2$ increased the specific surface area of the material and provided more active sites for the photocatalyst. The utilization of tin precursor significantly influences the specific surface area of the composites. Composites synthesized using SnCl$_4$·5H$_2$O exhibit the largest specific surface area, whereas those produced with Na$_2$SnO$_3$·3H$_2$O have the smallest specific surface area. This may be due to the fact that Sn^{4+} has a higher charge than Sn^{2+}. During the formation of the complex, Sn^{4+} may cause greater distortion in the lattice of SiO$_2$–TiO$_2$, thus creating more pores and defects within the material and increasing the specific surface area. In contrast, Sn^{2+} induces less lattice distortion.[12] For Na$_2$SnO$_3$, the SnO$_3^{2-}$ anion exhibits distinct structural and property characteristics compared to Sn^{4+} and Sn^{2+}. Consequently, it forms different chemical bonds and structures with SiO$_2$–TiO$_2$ in the system, which hinders the formation of structures with a high specific surface area.[28]
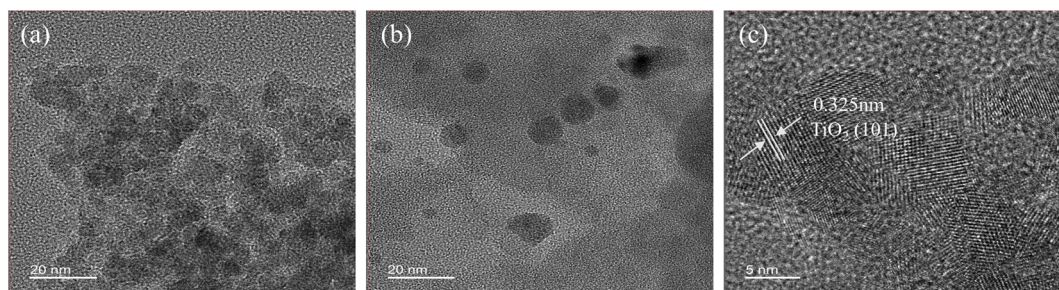

Fig. 4 TEM images of TiO$_2$/SnO$_2$ (SnCl$_4$) (a) and SiO$_2$–TiO$_2$/SnO$_2$ (SnCl$_4$) (b), HRTEM images of SiO$_2$–TiO$_2$/SnO$_2$ (SnCl$_4$) (c).

Table 1 Physicochemical properties of samples

Samples	S_{BET} (m² g⁻¹)	Band gap energy (eV)	Pore volume (cm³ g⁻¹)	Pore size (nm)
TiO_2	100.3152	3.32	0.1718	3.0606
TiO_2/SnO_2 ($SnCl_4$)	136.1575	2.92	0.1328	3.1390
SiO_2–TiO_2	442.9692	3.32	0.1914	2.7956
SiO_2–SnO_2 ($SnCl_4$)	484.9605	3.58	0.2632	4.6910
SiO_2–TiO_2/SnO_2 ($SnCl_4$)	272.1116	2.81	0.1838	2.6483
SiO_2–TiO_2/SnO_2 ($SnCl_2$)	180.7277	2.85	0.1200	2.8943
SiO_2–TiO_2/SnO_2 (Na_2SnO_3)	141.9377	2.87	0.1027	2.6569

To further investigate the chemical composition and binding states of the samples, the X-ray photoelectron spectroscopy of the samples was investigated. As shown in Fig. S4a, the binding energies of Ti $2p_{1/2}$ and Ti $2p_{3/2}$ in SiO_2–TiO_2/SnO_2 ($SnCl_4$) were located at 458.8 eV and 464.6 eV, respectively, attributed to Ti^{4+}.[29] The Sn 3d spectra of SiO_2–TiO_2/SnO_2 ($SnCl_4$) show spin–orbit double peaks at 495.6 eV and 486.8 eV, respectively, due to Sn^{4+} (Fig. S4b).[10] The binding energy of Si 2p in SiO_2–TiO_2/SnO_2 ($SnCl_4$) is located at 103.2 eV, attributed to Si^{4+} (Fig. S4c).[20] As shown in Fig. 5, the XPS curves of O 1s in SiO_2–TiO_2/SnO_2 ($SnCl_4$) can be identified as two peaks at 530.98 eV and 532.58 eV, which can be attributed to covalently bonded oxygen and surface oxygen species (Si–O, surface hydroxyl groups and adsorbed water) and metal oxide lattice oxygen (Sn–O and Ti–O).[30] Compared to Fig. 5a, it can be seen that the amount of covalently bonded oxygen and surface oxygen species increases with the addition of SiO_2. Firstly, the Si–O bond exhibits a peak at 532.58 eV, indicating that the introduction of SiO_2 directly enhances the signal at this energy level.[31] Secondly, the high specific surface area of SiO_2 may result in a greater amount of adsorbed water (H_2O) or hydroxyl residues, which in turn contributes to the increase of the 532.58 eV peak.[32] Surface adsorbed water and –OH groups can trap photogenerated holes (h^+) into reactive –OH radicals, thereby improving the photocatalytic performance of the materials.[33]

As can be seen from Fig. 4b, different tin precursors also influence the binding energy of O 1s. The O 1s binding energies of SiO_2–TiO_2/SnO_2 ($SnCl_4$) (532.58 eV and 530.98 eV) are higher than those of SiO_2–TiO_2/SnO_2 ($SnCl_2$) (532.28 eV and 530.68 eV) and SiO_2–TiO_2/SnO_2 (Na_2SnO_3) (532.28 eV and 530.58 eV). In SiO_2–TiO_2/SnO_2 ($SnCl_4$), compared to $SnCl_2$, Sn^{4+} carries a stronger positive charge which further polarises the Sn–O bond and reduces the electron density around oxygen, thereby increasing the O 1s binding energy. Sn^{2+} displays lower Lewis acidity and a diminished capacity to withdraw electron density from oxygen, resulting in a lower O 1s binding energy for SiO_2–TiO_2/SnO_2 ($SnCl_2$) O 1s.[34] As for SiO_2–TiO_2/SnO_2 (Na_2SnO_3), Na^+ ions inhibit the formation of the SnO_2 phase, maintaining the high purity Na_2SnO_3 structure. The O atoms in the SnO_3^{2-} group have a higher electron density, resulting in the lowest O 1s binding energy of the three samples. A higher binding energy signifies a reduced electron cloud density of the lattice oxygen in metal oxides (Sn–O, Ti–O), which enhances the oxidative capacity of holes (h^+) and facilitates the photocatalytic degradation of pollutants.[35]

3.2 Photocatalytic degradation of TC and CIP

The photocatalytic activity of the materials was assessed by evaluating the degradation of tetracycline (TC) and ciprofloxacin (CIP) at concentrations of 20 mg L⁻¹ under visible light irradiation. As illustrated in Fig. 6a and b, the incorporation of SiO_2 and different tin precursors significantly influenced the removal efficiency of tetracycline (TC) and ciprofloxacin (CIP). Among the tested composites, SiO_2–TiO_2/SnO_2 ($SnCl_4$) exhibited the highest removal rates for TC and CIP (84.9% and 81.3%), achieving a performance more than 1.5 times greater than that of TiO_2/SnO_2 ($SnCl_4$) (57% and 54%). Notably, composites prepared using $SnCl_4$ as the tin precursor exhibited superior removal efficiency compared to those synthesized with $SnCl_2$ or $Na_2SnO_3 \cdot 3H_2O$. Furthermore, SiO_2–SnO_2 ($SnCl_4$) and SiO_2–TiO_2 displayed significant adsorption capabilities (Fig. S3), which can be attributed to their high specific surface areas (484.9605 and 442.9692 m² g; see Table 1). Despite their strong adsorption properties, the photocatalytic degradation performance of SiO_2–SnO_2 ($SnCl_4$) and SiO_2–TiO_2 under visible light is constrained by the wide band gaps of TiO_2 and SnO_2.

The kinetic analysis of TC and CIP degradation was based on the fitting of pseudo-first-order equations, and the kinetic constants are shown in Fig. 7, with K values for the materials listed in Table 3. Among the catalysts tested, SiO_2–TiO_2/SnO_2
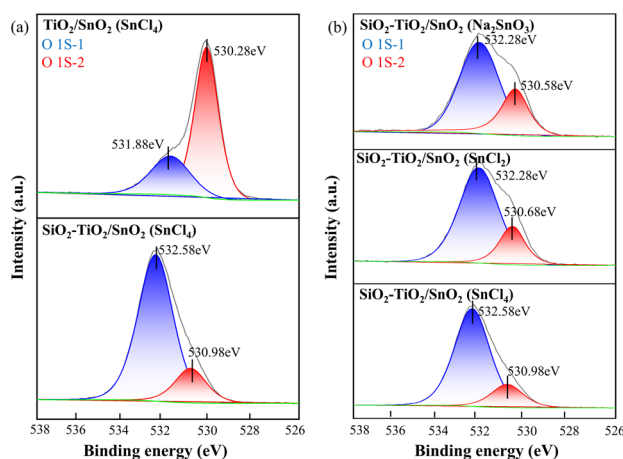

Fig. 5 XPS spectra of O 1s region for samples, (a) the influence of SiO_2, (b) the influence of Sn precursors.
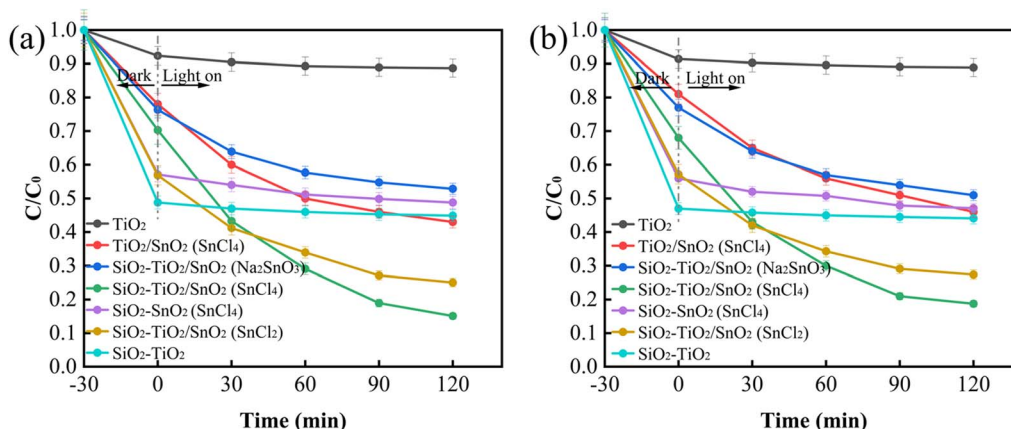
Fig. 6 Removal curves of TC (20 mg L⁻¹) (a) and CIP (20 mg L⁻¹) (b) with error bars represent the standard deviation from three measurements, replace "−120" with "−30" for aesthetics in the horizontal coordinates of the figure.

(SnCl₄) exhibited the highest K values, with values of 0.0130 min⁻¹ for the photocatalytic degradation of TC and 0.0110 min⁻¹ for the photocatalytic degradation of CIP, respectively. The higher K value showed that the material degraded faster. Notably, the K value for TC was 1.88 and 4.33 times higher than those of composites prepared with SnCl₂ and Na₂SnO₃·3H₂O as tin precursors, respectively. Furthermore, the incorporation of SiO₂ resulted in a significant enhancement of the photocatalytic degradation rate, achieving a 2.65-fold increase in the K value for the degradation of TC compared to the TiO₂/SnO₂ (SnCl₄). These results underscore the critical role of SiO₂ incorporation and tin precursor selection in optimizing the degradation efficiency of TC and CIP.

Additionally, comparisons with previous studies have been conducted to evaluate the photocatalytic performance, as presented in Tables 2 and 4. Like Tables 2 and 4, TC and CIP were identified as the selected degradants in this study, and the prepared composites showed high removal of both compounds in visible light compared to previous studies.

3.3 Mechanism

It is essential to evoke some reasons about the SiO₂–TiO₂/SnO₂ (SnCl₄) exhibited high performance in photocatalytic degradation

of TC and CIP under visible light, though the mechanism is still far from understood. A series of spectroscopic and electrochemical analyses were systematically conducted to characterize the samples, including transient photocurrent measurements, electrochemical impedance spectroscopy (EIS), photoluminescence (PL) spectroscopy, and ultraviolet-visible (UV-vis) diffuse reflectance spectroscopy. The corresponding experimental results are comprehensively presented in Fig. 8a–d.

As shown in Fig. 8, the SiO₂–TiO₂/SnO₂ (SnCl₄) composites exhibit the highest transient photocurrent intensity (Fig. 8a) and the smallest electrochemical impedance spectroscopy arc radius (Fig. 8b), indicating excellent charge separation efficiency and minimum charge transfer resistance. The photoluminescence (PL) spectra (Fig. 8c) showed that the emission peak intensity of SiO₂–TiO₂ was significantly reduced compared to that of pure TiO₂, whereas the weakest PL signal was obtained for SiO₂–TiO₂/SnO₂ (SnCl₄), confirming the effective suppression of charge recombination. The UV-vis absorption spectra (Fig. 8d) showed that the absorption edges of all the tin-containing samples were red-shifted, with SiO₂–TiO₂/SnO₂ (SnCl₄) having the widest absorption region with a band gap of 2.81 eV (the band gap of the prepared samples was estimated from the Tauc plot as shown in Fig. S5).
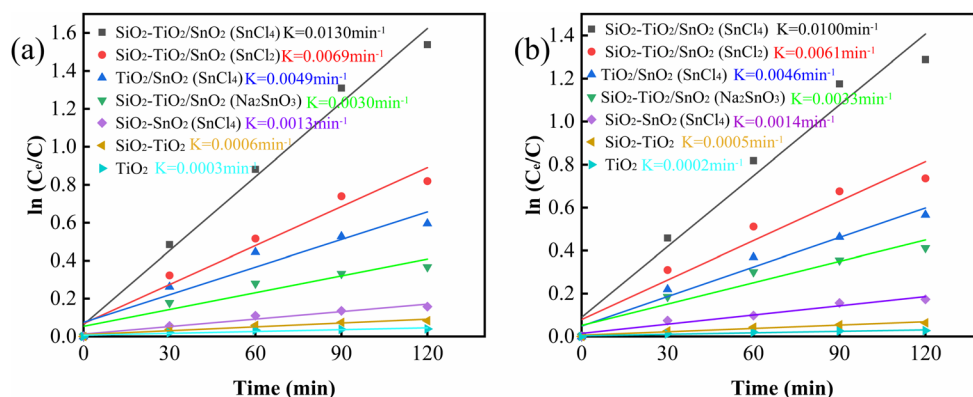

Fig. 7 Apparent first order rate constant k (min⁻¹) for TC (20 mg L⁻¹) (a) and CIP (20 mg L⁻¹) (b) photocatalytic degradation over the as-prepared samples.

Table 2 Lists a variety of photocatalysts for TC degradation

Sample names	Dosage (g L^{-1})	Concentration (mg L^{-1})	Time (min)	Removal rate (%)	Reference
N–TiO$_2$	0.2	10	120	87.0	36
BiOIO$_3$/BiOBr	0.8	20	80	74.9	37
Bi/BiVO$_4$	0.5	10	60	74.7	38
TiO$_2$–ZnO	2.5	10	165	99.1	39
This work	0.4	20	240	84.9	—

Table 3 The corresponding kinetic constant of TC and CIP degradation (except for adsorption)

Samples	K (TC, min^{-1})	K (CIP, min^{-1})
TiO$_2$	0.0003	0.0002
SiO$_2$–TiO$_2$	0.0006	0.0005
SiO$_2$–SnO$_2$ (SnCl$_4$)	0.0013	0.0014
SiO$_2$–TiO$_2$/SnO$_2$ (Na$_2$SnO$_3$)	0.0030	0.0033
TiO$_2$/SnO$_2$ (SnCl$_4$)	0.0049	0.0046
SiO$_2$–TiO$_2$/SnO$_2$ (SnCl$_2$)	0.0069	0.0061
SiO$_2$–TiO$_2$/SnO$_2$ (SnCl$_4$)	0.0130	0.0100

In summary, these findings indicated that the mechanism underlying the enhancement of the photocatalytic properties of the materials primarily involves two factors: the incorporation of SiO$_2$ and the use of various tin precursors. The incorporation of SiO$_2$ significantly improved the photocatalytic performance through two main mechanisms. Firstly, as shown in Fig. 8b and c, the incorporation of SiO$_2$ effectively reduced the electrochemical impedance and increased the intensity of the photoluminescence(PL) of the materials. This improvement can be attributed to the role of SiO$_2$ as a structural mediator, facilitating close contact between TiO$_2$ and SnO$_2$ to form a more efficient heterostructure. The resulting synergistic effect not only narrowed the band gap but also extended the visible light absorption while suppressing the recombination of photogenerated electron–hole pairs.[44] Secondly, as shown in Table 1 and Fig. 3, the incorporation of SiO$_2$ increased the specific surface area of the material and promoted a more looser structure. This structural modification provided additional active sites for photocatalytic reactions. Furthermore, the increased specific surface area improved light scattering efficiency, thereby increasing the material's overall light-harvesting capability. These combined effects synergistically contributed to the superior photocatalytic performance of the SiO$_2$-modified composites.[20]

Fig. 8 demonstrates that various tin precursors significantly influence both the rate of photogenerated electron–hole separation and the lifetime of photogenerated carriers. The photogenerated carrier lifetime of SiO$_2$–TiO$_2$/SnO$_2$ (SnCl$_4$) is greater than that of SiO$_2$–TiO$_2$/SnO$_2$ (SnCl$_2$) and also exceeds that of SiO$_2$–TiO$_2$/SnO$_2$ (Na$_2$SnO$_3$), indicating that the choice of tin precursor is crucial for the enhanced properties of the samples.

For the three tin precursors, Sn^{4+} in SnCl$_4$·5H$_2$O is more easily converted to SnO$_2$ and forms a heterojunction structure with TiO$_2$. This reduces the forbidden bandwidth, facilitates the enhancement of the separation rate of photogenerated carriers, reduces the complexation between photogenerated electrons and holes, and thus enhances the activity and strength of the photocatalyst.[45] Sn is in the +2 valence state in SnCl$_2$, likely due to incomplete oxidation. Although Sn in this state can influence the structure and properties of titanium dioxide, its ability to transfer and transmit electrons during the photocatalytic process is relatively weak because of its low valence.[12] Tin exhibits a +4 oxidation state in Na$_2$SnO$_3$·3H$_2$O; however, the presence of a substantial amount of sodium ions (Na$^+$) in the system plays a crucial role. Na$^+$ ions can inhibit the formation of the SnO$_2$ phase, thereby preserving the high purity phase structure of Na$_2$SnO$_3$·3H$_2$O, which is not favourable for the formation of TiO$_2$/SnO$_2$ heterojunctions.[46]

Free radical trapping tests were carried out on SiO$_2$–TiO$_2$/SnO$_2$ (SnCl$_4$) as shown in Fig. 9a and b to determine which are the active species in the photocatalytic process of SiO$_2$–TiO$_2$/SnO$_2$ (SnCl$_4$). The photodegradation efficiency decreased when Isopropanol (IPA), ethylenediamine tetraacetic acid disodium salt (EDTA-2Na), and p-benzoquinone (BQ) were added to the TC and CIP solutions. The degradation efficiencies decreased to 54.7% and 49.9% with the addition of IPA, 62.9% and 60.7% with the addition of EDTA-2Na, and 77.4% and 77.3% with the addition of BQ. This result indicates that ·OH and h$^+$ are the main active species of SiO$_2$–TiO$_2$/SnO$_2$ (SnCl$_4$) photocatalysts during the photodegradation of CIP and TC. To verify this

Table 4 Lists a variety of photocatalysts for CIP degradation

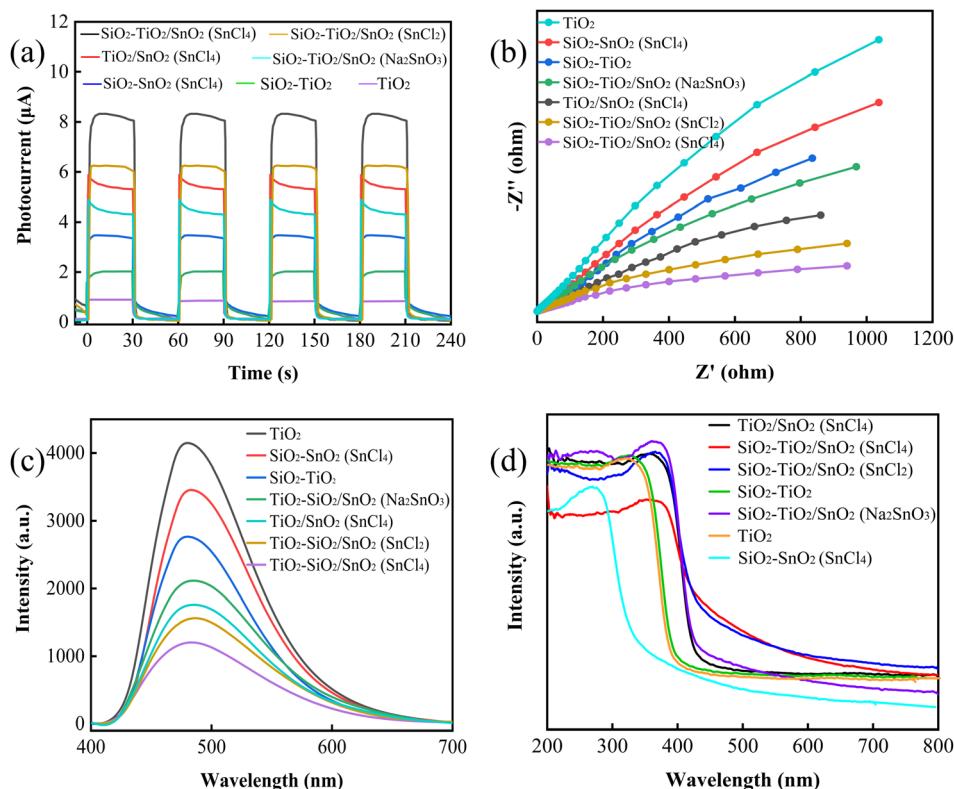| Sample names	Dosage (g L^{-1})	Concentration (mg L^{-1})	Time (min)	Removal rate (%)	Reference
Zn–Cu$_2$O	0.6	20	270	94.6	40
C–TiO$_2$	1.0	50	360	35.0	41
BiOCl/Si	0.5	10	240	94.0	42
TiO$_2$/g-C$_3$N$_4$	0.2	10	60	93.4	43
This work	0.4	20	240	81.3	—

Fig. 8 (a) Transient photocurrent. (b) Nyquist plots of EIS. (c) PL spectra and. (d) UV-vis diffuse reflectance spectra.

conclusion, electron paramagnetic resonance (EPR) spectroscopy is shown in Fig. 9c. In the absence of light, the EPR spectra in Fig. S6 do not show any distinct signal peaks. After 10 minutes of irradiation under a 500 W xenon lamp, the EPR spectrum of $SiO_2–TiO_2/SnO_2$ ($SnCl_4$) shows four distinct peaks in the range of 3460 to 3560 G, which corresponds to the characteristic signals of $\cdot OH$.[20] The EPR results confirm that $SiO_2–TiO_2/SnO_2$ is capable of generating $\cdot OH$ in the presence of light.

To assess the reusability of the $SiO_2–TiO_2/SnO_2$ ($SnCl_4$) photocatalyst, a series of four reusability tests was conducted. The results are shown in Fig. 10a and b. After four cycles, the degradation rate of $SiO_2–TiO_2/SnO_2$ ($SnCl_4$) for TC and CIP changed from 84.9% and 81.3% to 81.0% and 77.5%, indicating that the photocatalyst has good stability in both TC and CIP

degradation. The sample demonstrates excellent reusability as a photocatalyst.

In order to investigate the degradation process of CIP and TC, liquid chromatography-mass spectrometry (LC-MS) was used to analyse the major degradation products of CIP and TC. Three possible degradation pathways were detected for CIP, as shown in Fig. S6: (1) in pathway 1, the secondary amines on the piperazyl ring were first attacked. Subsequently, the carbon–nitrogen bonds broke down.[47] (2) In pathway 2, the $m/z = 348$ organic matter was generated by CIP.[48] (3) Pathway 3 was generated by CIP through the free radical elimination of CO, which then evolved through oxidation.[16] As shown in Fig. S7, two possible degradation pathways for TC were identified. Pathway 1 could involve the dehydration of the TC molecule to generate an intermediate product with a mass-to-charge ratio
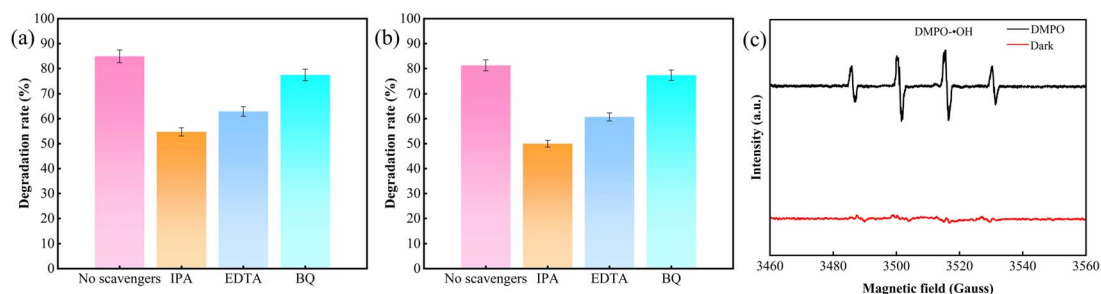

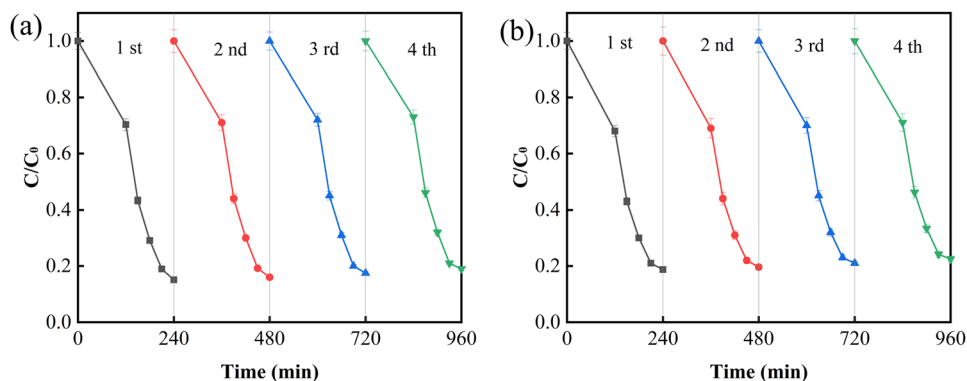**Fig. 9** Free radical capture experiment TC (a), CIP (b). EPR spectra of $SiO_2–TiO_2/SnO_2$ ($SnCl_4$) (c).

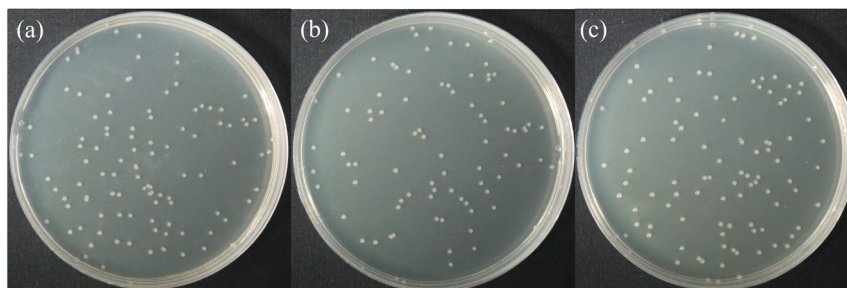**Fig. 10** Recycling tests of degradation TC (a) and CIP (b) using SiO_2-TiO_2/SnO_2 (SnCl$_4$).

Fig. 11 Effect of *E. coli* activity: (a) blank control, (b) ciprofloxacin solution before degradation, (c) degraded ciprofloxacin solution.

(m/z) of 427, followed by a deamination reaction leading to the formation of an intermediate product with an m/z of 410. This intermediate product undergoes terminal oxidation induced by H^+, $\cdot O_2^-$ and $\cdot OH$, resulting in an intermediate product with an m/z of 302.[49] (2) Pathway 2 may involve attack by $SO_4^- \cdot$ radicals, generating a product with $m/z = 461$, which is then further oxidised to produce a product with $m/z = 477$.[50] The total organic carbon (TOC) removal experiments are shown in Table S1. The mineralisation of ciprofloxacin (CIP) and tetracycline hydrochloride (TC) was 29.46% and 33.11% respectively (see Table S1). This indicated that CIP and TC were partially mineralised to CO_2 and H_2O.

It is essential to assess the toxicity of the solution after photocatalytic treatment.[51] As shown in Fig. 11, the toxicity of the treated solution was determined by comparing the effect of the solution on the viability of *E. coli* before and after the treatment by means of the *E. coli* viability assay. The plate smear count test was used to record the number of colonies. Fig. 11 shows that there were 101 colonies in the blank group, 84 in the pre-treatment solution group, and 97 in the post-treatment solution group. This suggests that the photocatalytically treated solution was essentially non-toxic to *E. coli*.

4 Conclusions

In this study, SiO_2-TiO_2/SnO_2 catalysts were successfully synthesized using different tin precursors (SnCl$_4\cdot$5H$_2$O, SnCl$_2$, Na$_2$SnO$_3\cdot$3H$_2$O) with emphasis on the role of SiO$_2$. The performance of the SiO_2-TiO_2/SnO_2 catalysts was evaluated for

the visible light-driven degradation of tetracycline (TC), and ciprofloxacin (CIP). Among the tested precursors, the catalyst derived from SnCl$_4\cdot$5H$_2$Oexhibited the highest photocatalytic activity, attributed to its small band gap and enhanced charge carrier separation. In addition, the incorporation of SiO$_2$ significantly improved the degradation efficiency, with the SiO_2-TiO_2/SnO_2 (SnCl$_4$) composite outperforming the TiO_2/SnO_2 (SnCl$_4$) composite without SiO$_2$. This improvement can be attributed to the role of SiO$_2$ in increasing the surface area, improving light absorption and inhibiting photogenerated electron–hole recombination. Free radical trapping experiments show that $\cdot OH$ and h^+ are the main reactants in the degradation process of TC and CIP. Repeated experiments showed that SiO_2-TiO_2/SnO_2 (SnCl$_4$) is a stable catalyst. These findings emphasize the importance of precursor selection and SiO$_2$ modification in the design of efficient heterogeneous photocatalysts for the degradation of PPCPs under visible light.

Author contributions

Kunyang Li: data curation, software, formal analysis, investigation, visualization, writing – original draft, writing – review & editing; Yidan Peng: formal analysis, validation; Shuangyu Li: software, validation; Fengying Luo: software, formal analysis; Jing Li: software, investigation; Haidong Ju: supervision, project administration; Yepeng Yang: supervision, project administration; Yizhou Li: conceptualization, resources, software, supervision, funding acquisition, methodology, writing – original draft, writing – review & editing, project administration. All

authors have read and agreed to the published version of the manuscript.

Conflicts of interest

The authors declare that they have no known competing financial interests or personal relationships that could appear to influence the work reported in this paper.

Data availability

The authors confirm that the data supporting the findings of this study are available within the article.

S1: instruments and equipment; S2: measurement of photocatalytic activity; S3: electron paramagnetic resonance (EPR) measurements; Fig. S1: surface area analysis of composites. N_2 adsorption/desorption isotherms of (a) TiO_2, (b) SiO_2–SnO_2 ($SnCl_4$); Fig. S2: surface area analysis of composites. N_2-adsorption/desorption isotherms of (a) TiO_2/SnO_2 ($SnCl_4$), (b) SiO_2–TiO_2/SnO_2 ($SnCl_4$), (c) SiO_2–TiO_2, (d) SiO_2–TiO_2/SnO_2 (-Na_2SnO_3), (e) SiO_2–TiO_2/SnO_2 ($SnCl_2$); Fig. S3: adsorption/desorption curves in the dark (a) TC, (b) CIP; Fig. S4: XPS spectra of Ti 2p, Sn 3d and Si 2p region for SiO_2–TiO_2/SnO_2 ($SnCl_4$); Fig. S5: plots of $(\alpha h\nu)^2 - h\nu$ (a–f); Fig. S6: proposed degradation pathway of CIP over SiO_2–TiO_2/SnO_2 ($SnCl_4$); Fig. S7: proposed degradation pathway of TC over SiO_2–TiO_2/SnO_2 ($SnCl_4$); Table S1: the total organic carbon (TOC) values of TC and CIP. See DOI: **https://doi.org/10.1039/d5ra03247d**.

Acknowledgements

References

1 J.-L. Liu and M.-H. Wong, *Environ. Int.*, 2013, **59**, 208–224.

2 W. Xu, G. Zhang, X. Li, S. Zou, P. Li, Z. Hu and J. Li, *Water Res.*, 2007, **41**, 4526–4534.

3 A. Kumar, M. Khan, L. Fang and I. M. C. Lo, *J. Hazard. Mater.*, 2019, **370**, 108–116.

4 Z. Cai, A. D. Dwivedi, W.-N. Lee, X. Zhao, W. Liu, M. Sillanpää, D. Zhao, C.-H. Huang and J. Fu, *Environ. Sci.: Nano*, 2018, **5**, 27–47.

5 C. S. L. Fung, M. Khan, A. Kumar and I. M. C. Lo, *Sep. Purif. Technol.*, 2019, **216**, 102–114.

6 A. Kumar, M. Khan, J. He and I. M. C. Lo, *Water Res.*, 2020, **170**, 115356.

7 H. Chen and J. Wang, *Chemosphere*, 2021, 269.

8 D. Liu, J. Zhou, J. Wang, R. Tian, X. Li, E. Nie, X. Piao and Z. Sun, *Chem. Eng. J.*, 2018, **344**, 332–341.

9 J. Wang, Z. Wang, D. Zhao, Y. Liang, H. Wang, N. Wang, W. Jiang, S. Liu, C. Liu, W. Ding and Z. Zhang, *Ceram. Int.*, 2022, **48**, 8297–8305.

10 P. Pascariu, C. Cojocaru, M. Homocianu, P. Samoila, C. Romanitan and D. Nikolay, *Ceram. Int.*, 2023, **49**, 10384–10394.

11 L.-R. Hou, C.-Z. Yuan and Y. Peng, *J. Hazard. Mater.*, 2007, **139**, 310–315.

12 K. Bila, T. Dontsova and A. Kutuzova, *Applications & Properties (NAP)*, 2020, 02NEE01-1–02NEE01-4.

13 S. E. Mousavi, H. Younesi, N. Bahramifar, P. Tamunaidu and H. Karimi-Maleh, *Chemosphere*, 2022, **297**, 133992.

14 M. Bellardita, M. Addamo, A. Di Paola, G. Marcì, L. Palmisano, L. Cassar and M. Borsa, *J. Hazard. Mater.*, 2010, **174**, 707–713.

15 M. r. S. Nivetha, J. V. Kumar, J. S. Ajarem, A. A. Allam, V. Manikandan, R. Arulmozhi and N. Abirami, *Environ. Res.*, 2022, **209**, 112809.

16 L. Jiang, Z. Luo, Y. Li, W. Wang, J. Li, J. Li, Y. Ao, J. He, V. K. Sharma and J. Wang, *Chem. Eng. J.*, 2020, **402**, 125549.

17 C. Mendoza, A. Valle, M. Castellote, A. Bahamonde and M. Faraldos, *Appl. Catal., B*, 2015, **178**, 155–164.

18 C. Wang, X. Wang, B.-Q. Xu, J. Zhao, B. Mai, P. a. Peng, G. Sheng and J. Fu, *J. Photochem. Photobiol., A*, 2004, **168**, 47–52.

19 A. K. Alves, F. A. Berutti and C. P. Bergmann, *Catal. Today*, 2013, **208**, 7–10.

20 S. Sun, H. Ding, L. Mei, Y. Chen, Q. Hao, W. Chen, Z. Xu and D. Chen, *Chin. Chem. Lett.*, 2020, **31**, 2287–2294.

21 V. S. Smitha, K. A. Manjumol, K. V. Baiju, S. Ghosh, P. Perumal and K. G. K. Warrier, *J. Sol–Gel Sci. Technol.*, 2010, **54**, 203–211.

22 J. Wang, J. Ge, H. Hou, M. Wang, G. Liu, G. Qiao and Y. Wang, *Appl. Surf. Sci.*, 2017, **422**, 970–974.

23 G. Pacchioni and H.-J. Freund, *Chem. Soc. Rev.*, 2018, **47**, 8474–8502.

24 C. Li, X. Zhou, Q. Zhang, Y. Xue, Z. Kuang, H. Zhao, C. Y. Mou and H. Chen, *ChemSusChem*, 2022, **15**, e202200188.

25 B. Singaram, J. Jeyaram, R. Rajendran, P. Arumugam and K. Varadharajan, *Ionics*, 2018, **25**, 773–784.

26 Y. He, L. Zhang, G. Chen, Y. Liu, S. Shi, P. Jiang, J. Ding, S. Xu and C. Geng, *Appl. Surf. Sci.*, 2023, **611**, 155724.

27 Z. A. ALOthman, *Materials*, 2012, **5**, 2874–2902.

28 S. Yao, S. Zhou, J. Wang, W. Li and Z. Li, *Photochem. Photobiol. Sci.*, 2019, **18**, 2989–2999.

29 I. Ullah, A. Haider, N. Khalid, S. Ali, S. Ahmed, Y. Khan, N. Ahmed and M. Zubair, *Spectrochim. Acta, Part A*, 2018, **204**, 150–157.

30 A. K. L. Sajjad, S. Shamaila and J. Zhang, *J. Hazard. Mater.*, 2012, **235**, 307–315.

31 B. M. Reddy, B. Chowdhury and P. G. Smirniotis, *Appl. Catal., A*, 2001, **211**, 19–30.

32 Y. Li, Y. Yang, P. Yang, L. Jiang, W. Wang, J. He, Y. Chen and J. Wang, *Catal. Commun.*, 2020, **145**, 106121.

33 Y. Changlin, Y. Kai, S. Qing, C. Y. Jimmy, C. Fangfang and L. Xin, *Chin. J. Catal.*, 2011, **32**, 555–565.

34 T. Liang, Z. Dai, Y. Liu, X. Zhang and H. Zeng, *Sci. Bull.*, 2021, **66**, 2471–2478.

35 Q. Zheng, E. Xu, E. Park, H. Chen and D. Shuai, *Appl. Catal., B*, 2019, **240**, 262–269.

36 S. Wu, H. Hu, Y. Lin, J. Zhang and Y. H. Hu, *Chem. Eng. J.*, 2020, **382**, 122842.

37 X. Kuang, M. Fu, H. Kang, P. Lu, J. Bai, Y. Yang and S. Gao, *Opt. Mater.*, 2023, **138**, 113690.

38 N. Kang, D. Xu and W. Shi, *Chin. J. Chem. Eng.*, 2019, **27**, 3053–3059.

39 S. Z. Heris, M. Etemadi, S. B. Mousavi, M. Mohammadpourfard and B. Ramavandi, *J. Photochem. Photobiol., A*, 2023, **443**, 114893.

40 X. Yu, J. Zhang, J. Zhang, J. Niu, J. Zhao, Y. Wei and B. Yao, *Chem. Eng. J.*, 2019, **374**, 316–327.

41 J.-W. Shi, Z. Wang, C. He, G. Li and C. Niu, *RSC Adv.*, 2015, **5**, 98361–98365.

42 Z. Jia, T. Li, Z. Zheng, J. Zhang, J. Liu, R. Li, Y. Wang, X. Zhang, Y. Wang and C. Fan, *Chem. Eng. J.*, 2020, **380**, 122422.

43 K. Hu, R. Li, C. Ye, A. Wang, W. Wei, D. Hu, R. Qiu and K. Yan, *J. Cleaner Prod.*, 2020, **253**, 120055.

44 F. Dai, Y. Wang, R. Zhao, X. Zhou, J. Han and L. Wang, *Int. J. Hydrogen Energy*, 2020, **45**, 28783–28791.

45 S. M. Hassan, A. I. Ahmed and M. A. Mannaa, *Ceram. Int.*, 2018, **44**, 6201–6211.

46 A. J. Kamble, P. P. Vhangutte, R. A. Madhale, P. D. Bhange, S. R. Patil and D. S. Bhange, *ChemistrySelect*, 2024, **9**, e202403317.

47 J. Deng, G. Wu, S. Yuan, X. Zhan, W. Wang and Z.-H. Hu, *J. Photochem. Photobiol., A*, 2019, **371**, 151–158.

48 X. Zheng, S. Xu, Y. Wang, X. Sun, Y. Gao and B. Gao, *J. Colloid Interface Sci.*, 2018, **527**, 202–213.

49 J. Song, Y. Yang, N. Cui, S. Sadiq, I. Khan, S.-y. Liu and K. Qi, *J. Water Proc. Eng.*, 2024, **68**, 106516.

50 Y. Zhang, J. Zhou, X. Chen, L. Wang and W. Cai, *Chem. Eng. J.*, 2019, **369**, 745–757.

51 J. He, J. Cheng and I. M. C. Lo, *Water Res.*, 2021, **190**, 116705.